

Hypersonic flow control of shock wave/turbulent boundary layer interactions using magnetohydrodynamic plasma actuators^{*}

Hao JIANG[†], Jun LIU, Shi-chao LUO, Jun-yuan WANG, Wei HUANG

Science and Technology on Scramjet Laboratory, National University of Defense Technology, Changsha 410073, China

[†]E-mail: jiangjeb@163.com

Received Jan. 17, 2020; Revision accepted June 5, 2020; Crosschecked Aug. 28, 2020

Abstract: The effect of magnetohydrodynamic (MHD) plasma actuators on the control of hypersonic shock wave/turbulent boundary layer interactions is investigated here using Reynolds-averaged Navier-Stokes calculations with low magnetic Reynolds number approximation. A Mach 5 oblique shock/turbulent boundary layer interaction was adopted as the basic configuration in this numerical study in order to assess the effects of flow control using different combinations of magnetic field and plasma. Results show that just the thermal effect of plasma under experimental actuator parameters has no significant impact on the flow field and can therefore be neglected. On the basis of the relative position of control area and separation point, MHD control can be divided into four types and so effects and mechanisms might be different. Amongst these, D-type control leads to the largest reduction in separation length using magnetically-accelerated plasma inside an isobaric dead-air region. A novel parameter for predicting the shock wave/turbulent boundary layer interaction control based on Lorentz force acceleration is then proposed and the controllability of MHD plasma actuators under different MHD interaction parameters is studied. The results of this study will be insightful for the further design of MHD control in hypersonic vehicle inlets.

Key words: Hypersonic; Shock wave/turbulent boundary layer interaction; Magnetohydrodynamic (MHD); Flow control
<https://doi.org/10.1631/jzus.A2000025>

CLC number: V211.48

1 Introduction

As hypersonic vehicles become able to reach higher Mach numbers (Ma) in the relatively lower layers of near space, the shock wave/turbulent boundary layer interaction (STBLI) of internal and external aerodynamics become more obvious (Zhang et al., 2019; Huang et al., 2020). Oblique STBLI is a typical configuration for the intake of hypersonic vehicles; this means that the strong adverse pressure gradient brought about by the compression wave system of intake causes the boundary layer to separate and generate complex and unsteady wave systems.

This phenomenon then leads to a burst of energy loss and degraded performance, even failure to start the scramjet engine. In order to avoid such negative effects, the bleed method (Sriram and Jagadeesh, 2014; Gaitonde, 2015) is now applied to reduce the separation zone while the loss of flow and the discharge system of high-temperature gas are two key factors that restrict efficacy.

Various passive and active approaches have been explored to delay or suppress STBLI-induced separation, including micro-vortex generators (Babinsky et al., 2009) and plasma (Zhou et al., 2017; Gan et al., 2018). Micro-vortex generators promote momentum transfer via counter-rotating vortices in the wake flow of the structure immersed inside the turbulent boundary layer. These structures must be placed optimally while the location of the flow separation is not fixed. Plasma control, in contrast, involves deposited energy as well as regulated additional

^{*} Project supported by the National Key R&D Program of China (Nos. 2019YFA0405300 and 2019YFA0405203) and the Chinese Scholarship Council (CSC) (No. 201903170195)

 ORCID: Hao JIANG, <https://orcid.org/0000-0001-7251-7875>

© Zhejiang University and Springer-Verlag GmbH Germany, part of Springer Nature 2020

momentum as part of the flow, providing a quick and adaptable response according to different incoming conditions. No moving parts are needed with plasma control, limiting the aerodynamic penalty when actuators are deactivated.

Different types of plasma techniques (e.g. direct current, alternating current, radio frequency, microwave, arc, corona, and spark discharge actuators) (Adamovich, 2010; Poggie et al., 2015) manipulate the flow field using two primary mechanisms, the generation of a body force and thermal effects. Amongst these plasma techniques, magnetohydrodynamic (MHD) has potential within the high-speed flow control field because the coupling of both a magnetic field and plasma provides a volume force (Lorentz force) that is several times larger than that of ion wind. It is noteworthy that the air encountered in hypersonic flight is highly ionized subsequent to bow shock in front of the blunt body and no artificial ionization is required for MHD control for flow fields with $Ma > 12$ (Li et al., 2017a). In contrast, MHD effects in a relatively cold hypersonic flow under a flight Ma of approximately 12 can only be significant using artificial ionization such as electric discharges to amplify air conductivity and provide directional current. A specific magnetic field and electric discharges constitute the MHD plasma actuator, used as the control device in this research on Mach 5 flow.

A range of recent experiments and simulations have been carried out on the supersonic boundary layer and separation control using MHD plasma actuators. In some examples, Meyer et al. (2004), Zaidi et al. (2006), and Saito et al. (2008) conducted MHD boundary layer control experiments in wind tunnels at Mach 3, Mach 2.8, and Mach 1.5. Experimental results showed that MHD had the effect of increasing the momentum and attenuating the density fluctuations of the boundary layer. Subsequent experiments were then performed to investigate the effects of a magnetized plasma column on supersonic boundary layer separation; acetone planar laser scattering images show that separation can be fully suppressed when magnetic field strengths and current intensities exceeded 3 T and 80 mA, respectively (Kalra et al., 2011). Similarly, Su et al. (2010) carried out laminar and $k-\omega$ shear stress transport (SST)-based turbulence numerical simulations on the MHD control of shock wave/boundary layer interaction separated flow, while Bisek et al. (2013) used the large-eddy simulation

method to study the STBLI of incoming flow at the Mach 2.25 and 24° compression corner. These results reveal that the thermal effects of plasma had little effect on control of the separation bubble at the compression corner, while Lorentz force reduced both the size of the separation zone and the turbulent kinetic energy. Atkinson et al. (2012) used the Spalart-Allmaras (SA) model to conduct experimental and numerical simulations of 3D STBLI considering side wall effects. These results show that the most important role of the actuator is to redistribute the separation vortex and that the 3D control method was more effective than that envisaged from initial 2D flow control results. Although some numerical and experimental studies of MHD control in supersonic STBLI have been carried out, the control mechanism incorporating a quantization parameter has not been investigated in detail, especially in the hypersonic STBLI flow field which requires stronger control than in supersonic flow. An improved MHD parameter in STBLI is needed to further interpret the MHD control mechanism as well as to predict actuator controllability.

An MHD solver based on a low magnetic Reynolds number solver was initially validated in this study using magnetically-controlled laminar flat plate flow and turbulent boundary layer calculations. A baseline case was then modeled according to the experimental setup of Schülein (2006). Actuator model parameters were taken from Kalra et al. (2009)'s experiments and a few assumptions were made to set up the time-averaged approach. The definitions of old MHD parameters are listed and a novel one is proposed using theoretical analysis. Flow controllability was then investigated based on several factors, including the thermal effect, MHD control position, and MHD interaction parameters. These results might be helpful in the future design and application of the MHD actuator in inlets on selecting the effective location and electrical input.

2 Physical model and numerical approach

2.1 Physical model

The physical model used here adopts a configuration from Schülein (2006)'s experiment, specifically the interactions between oblique shock produced by a $\beta=14^\circ$ wedge and a turbulent hypersonic

boundary layer. The surface pressure and friction coefficient provided in (Schülein, 2006) were used here as these prove to be adequate experimental data for hypersonic STBLI (Brown, 2011). Smaller wedge angles are not sufficient to cause separation under these inflow conditions. The reference conditions for the baseline flow are listed in Table 1. Fig. 1 illustrates the flow field configuration and boundary conditions used in this study.

Table 1 Reference conditions for baseline flow

Parameter	Value	Parameter	Value
Ma	5	P_∞ (Pa)	4006.8
T_∞ (K)	68.33	Re/m	3.6737×10^7
T_w (K)	300		

T_∞ and T_w are the temperatures of the main flow and the wall, respectively; P_∞ is the pressure of the main flow

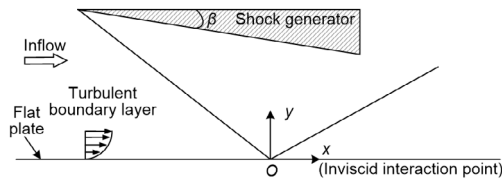


Fig. 1 Baseline configuration

2.2 Numerical method

The full MHD equation set includes a complicated coupling of Maxwell’s equations, generalized Ohm’s law, and the Navier-Stokes equation. However, for typical hypersonic flows, the low magnetic Reynolds number ($Re_\sigma \ll 1$) approximation allows for a simple form embodying electromagnetic effects in the source terms of the momentum and energy equations.

The dimensional governing equations in Cartesian coordinates are expressed as follows:

$$\frac{\partial \mathbf{U}}{\partial t} + \frac{\partial \mathbf{F}}{\partial x} + \frac{\partial \mathbf{G}}{\partial y} + \frac{\partial \mathbf{H}}{\partial z} = \frac{\partial \mathbf{F}_v}{\partial x} + \frac{\partial \mathbf{G}_v}{\partial y} + \frac{\partial \mathbf{H}_v}{\partial z} + \mathbf{S}_{\text{MHD}}, \quad (1)$$

$$\mathbf{U} = [\rho \quad \rho u \quad \rho v \quad \rho w \quad \rho e_t]^T, \quad (2)$$

where t is the time, x , y , and z are the dimensional coordinates, \mathbf{F} , \mathbf{G} , and \mathbf{H} are the inviscid fluxes, and \mathbf{F}_v , \mathbf{G}_v , and \mathbf{H}_v are the viscous fluxes. The source vector \mathbf{S}_{MHD} is on the right. ρ is the gas density, u , v , and w are the velocity components, and e_t is the total energy per unit mass.

As the incoming flow is hypersonic, computational predictions adopt a compressible flow solver with the turbulence model of $k-\omega$ SST and SA. The finite volume method was used to discretize the Reynolds-averaged Navier-Stokes (RANS) equations, a second-order upwind Roe scheme is adopted for spatial difference, and the time term is solved using a lower-upper symmetric Gauss-Seidel (LU-SGS) implicit time integration method. The air model assumes a perfect gas with a specific heat ratio of 1.4; viscosity and heat conductivity all obey Sutherland’s law. Uniform flow is used to initialize the flow field. The uncontrolled baseline state is calculated, and then the source terms of MHD effects are added into the calculation. The calculation is stopped after monitoring converges to a total residual decline of more than three orders of magnitude and the minimum mass flux difference between inflow and outflow reaches 0.005 kg/s.

2.3 Actuator model

Arc discharge is a strong self-sustaining discharge in gas that leads to considerable conductivity between electrodes. Previous experiments on MHD control of supersonic STBLI have used this method to produce plasma above the surface, called a ‘snow-pow arc’ (Kalra et al., 2009).

According to the relative direction of incoming flow and the electrode arrangement, current research on plasma arc discharge for high-speed flow control can be divided into two types, longitudinal and transversal distributions (Leonov et al., 2002; Shang and Surzhikov, 2005).

The summary in Fig. 2 shows the transversal arrangement of two electrodes embedded on the surface of a controlled area, along with the uniform and vertical magnetic field in (Kalra et al., 2009)’s experiment and our research. The directional combination of arc discharge and magnetic field could vary in different ways, which may generate 3D effects, not covered in this analysis. The external magnetic field is applied in $+y$ direction and the external electrical field is applied in $-z$ direction. Discharge electrodes are made of 0.1 mm-thick aluminum foil buried under the wall surface, and they are slightly expanded by an angle of 0.6° along the flow direction. The anode is grounded, and the cathode is connected to the power supply through a ballast resistor.

Moving arc images were captured by high-speed photography (Zaidi et al., 2006) shown in Fig. 3a and a 2D schematic diagram of this process is presented in Fig. 3b. The discharge process and the interaction between plasma and air can be described as follows. A diameter of approximately 1 mm firstly forms at the narrowest side of the diverging electrodes after a large voltage is applied. Then the plasma column sweeps downstream and it is not extinguished until reaching the end of the electrodes, after which it is ignited again at the front. It appears to the eye that the entire region between the electrodes is occupied by a uniform discharge.

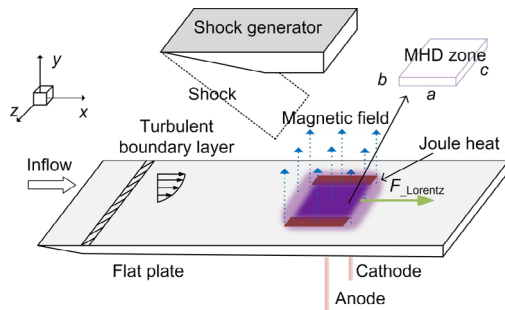


Fig. 2 MHD plasma actuator model
a: length; b: height; c: width

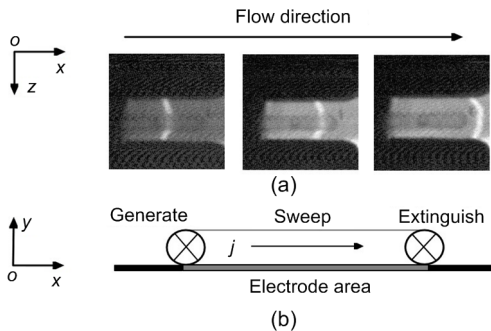


Fig. 3 High-speed photographs of the arc movement downstream at $B=0$ T in (Zaidi, 2006)'s experiments (a) and 2D schematic diagram of arc movement (b)

A further measurement of arc velocity under the uniform magnetic field was done using microsecond exposures which indicated that the Lorentz force ($F_{Lorentz}$) downstream helped the arc propagate much faster with a 2.0-T magnetic field. This rate is faster than that which would have been observed in the absence of the field. The arc was canted at an average angle of 60° – 70° with respect to the streamwise direction as the magnetic field was applied (Zaidi et al.,

2006). The plasma column acts like a porous piston (Macheret, 2006) moving downstream. Although the ion and electron move at the same velocity, the momentum transporting air molecules is attributed to the collision of ions to molecules because the ion momentum exceeds electron momentum by more than four orders of magnitude. The actuator model we propose is based on three assumptions:

(a) There is a frequent moving arc inside the MHD interaction zone converting input power into mechanical work and Joule heat, shaped like a column which neglects the canting angle. The constant current and voltage are sustained in a stabilized mode between the anode and cathode.

(b) The Hall effect is not considered because the force due to polarization electric field inside the arc is too small compared to the Lorentz force.

(c) The MHD interaction is deemed as a quasi-steady state in RANS simulations. As the frequency of the repeated and magnetically-driven arc could be as high as 100 kHz in experiments, which is orders of magnitude larger than the characteristic frequency of the fluid. The cuboid-shaped MHD interaction zone shown in Fig. 2 approximately represents the spatial region of arc column motion. A uniform conductivity of the MHD zone is taken as that of the moving column while the Joule heat is evenly distributed in the whole MHD zone.

On the basis of experimental results and the assumptions above, an actuator was incorporated in the fluid using time-mean source terms. The momentum exchange and Joule heat in the MHD zone from the actuator were then semi-empirically modeled as a steady and uniform heat source and a magnetic body-force term in the momentum and energy equations, respectively. The MHD zone is assumed to be a cube with length, height, and width of $a=22$ mm, $b=1$ mm, and $c=11$ mm, respectively (Kalra et al., 2009); this zone is located in the specific location of the computation domain where the source term is activated. The source term can be expressed as follows:

$$\mathbf{S} = \begin{bmatrix} 0 \\ f_x \\ f_y \\ f_z \\ q + uf_x + vf_y + wf_z - q_{vb} \end{bmatrix}, \quad (3)$$

$$f_x = \sigma \left[B_z (E_y + wB_x - uB_z) - B_y (E_z + uB_y - vB_x) \right], \quad (4)$$

$$f_y = \sigma \left[B_x (E_z + uB_y - vB_x) - B_z (E_x + vB_z - wB_y) \right], \quad (5)$$

$$f_z = \sigma \left[B_y (E_x + vB_z - wB_y) - B_x (E_y + wB_x - uB_z) \right], \quad (6)$$

where E_x, E_y, E_z , and B_x, B_y, B_z denote components of the electric field strength \mathbf{E} and the magnetic field \mathbf{B} in the three directions x, y , and z , respectively. σ is the conductivity of the plasma arc column between the electrodes following theoretical analysis (Kalra et al., 2009). The terms f_x, f_y , and f_z are Lorentz force components, while q is the Joule heat, and q_{vb} is the vibrational energy. This translates to

$$q = \frac{VI}{abc} - (uf_x + vf_y + wf_z), \quad (7)$$

where V is the voltage across the discharge electrode, I is the circuit current intensity. As only the electric field in the z direction is considered, then

$$E_z = -\frac{V}{c}, \quad (8)$$

$$E_x = E_y = 0, \quad (9)$$

$$\sigma = \frac{I}{\frac{V}{c} \cdot \frac{\pi b^2}{4}}. \quad (10)$$

Experimental and analysis results show that $E_z = -1.2$ kV/cm and $I = 35-250$ mA. The reason why the vibrational energy was subtracted from the source term of the energy equation is that during the process of plasma discharge, most energy of Joule heat primarily participates in the process of vibration excitation, while the other small part goes into gas heating. The ratio between vibration excitation energy and total deposited energy is defined as χ ; thus, after weakly ionized gas exits the MHD control zone and continues to flow downstream, electrons, ions, and other components gradually recombine and vibration energy is released in the form of heat. The estimated characteristic time for this process usually exceeds 10 ms. The STBLI zone is therefore far away from the

influence of recombination. We assume $\chi = 95\%$ as shown in (Bisek and Poggie, 2013) and rewrite Eq. (3) as

$$\mathbf{S} = \begin{bmatrix} 0 \\ f_x \\ f_y \\ f_z \\ (1-\chi)q + uf_x + vf_y + wf_z \end{bmatrix}. \quad (11)$$

The actuator model proposed here heavily relies on experimental data and the simplifications of the unsteady process, which may be flawed in some respects such as changed discharge characteristics in different flow conditions or the improper modeling of dynamic processes. More detailed work should be done in the future to develop a more sophisticated model that can account for plasma formation, gas and cathode heating, gas flow, and electron emission processes (Richard et al., 1996; Kolev and Bogaerts, 2014). In terms of the MHD interaction parameters described later in this paper, actuator effects are only represented by the conductivity and the length of the MHD region. Thus, if we replace the present conductivity with the conductivity in a more accurate model in the future, we will achieve better control prediction from the input electrical parameters. The effects of heated electrodes on the wall temperature might well be included in further study although we can use active control to cool the electrodes down.

2.4 Code validation

In order to guarantee the accuracy of the solver's Lorentz source term, supersonic conductive flows over a 0.08-m long flat plate were computed and the boundary layer velocity profile at $x = 0.06$ m was compared with the reference results proposed by Dietiker and Hoffmann (2002). Flow conditions are $Ma = 2$, $T = 300$ K, adiabatic wall, $Re = 3.75 \times 10^6$, conductivity $\sigma = 800$ S/m, and magnetic field $B = 1$ T. The direction is vertical upwards in this experiment. The summary in Fig. 4 gives a comparison of computed results with the referred results, where the x -axis is the non-dimensional x -velocity and the y -axis is the non-dimensional wall distance (reference length L is the length of the flat plate), and proves the ability of this solver to compute MHD flow given the low magnetic Reynolds number assumption.

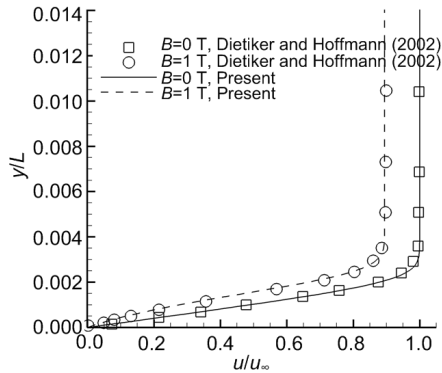


Fig. 4 Boundary layer velocity profile at $x=0.06$ m

To validate the hypersonic STBLI simulation used in this solver, we compared simulation results with experimental ones from Schülein (2006). The flow field in the experiment was a fully turbulent flow. The angle of the shock generator was 14° and the separation of the boundary layer in the corresponding flow field was strong. Identical flow fields in experiments were simulated with a grid amount of 480×150 , and y^+ of the first layer was below 1. Numerical results using both SA and SST turbulence models are compared with experimental results in Figs. 5 and 6.

Fig. 5 reveals the wall static pressure distributions along the streamwise direction from SA and SST computational results compared with experimental data. The SA turbulence model was able to capture the right rising point of pressure and both models under-predict the plateau pressure. Fig. 6 shows the wall skin friction coefficient distributions from the SA and SST computational results compared with experimental data (Schülein, 2006). The x -axis area corresponding to the y -axis value below zero represents the separation zone; separation length from experiments, the SA turbulence model, and the SST turbulence model are 0.034 m, 0.036 m, and 0.432 m, respectively. Although the two turbulence models both have limitations in the simulation of the reattachment flow (Zhou et al., 2019), the SA turbulence model prediction is better at revealing separation length. We chose to use the SA turbulence model in this research.

We compared the Mach 5 turbulent boundary layer profile of the baseline flow field inlet, computed by the SA turbulence model under the same grid as well as another typical flow of Mach 2.25. Direct

numerical simulation (DNS) data of compressible boundary layer were taken from Pirozzoli et al. (2004) as well as the van Driest law of the wall (Fig. 7). Computational results are coincident with DNS data and theory. It is clear that the van Driest transformed velocity from simulation results exceeds 21 when $y^+ > 400$, proving a fully turbulent boundary layer (White, 1991). The results of wall static pressure, skin friction coefficient distribution, and the inner layer of the van Driest profile imply that the number of cells is sufficient for this investigation.

The non-dimensional parameters in the van Driest transformation are as follows:

$$y^+ = \frac{\rho_w u_\tau y}{\mu_w}, \tag{12}$$

$$u^+ = \frac{u}{u_\tau}, \tag{13}$$

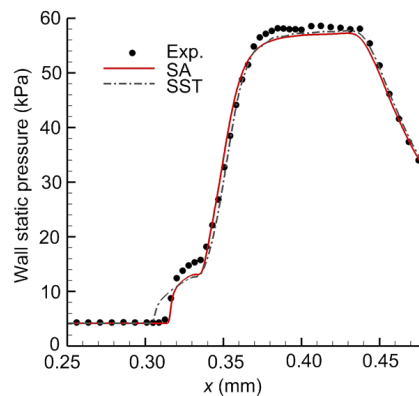


Fig. 5 Wall static pressure distributions from SA and SST computational results compared with experimental data

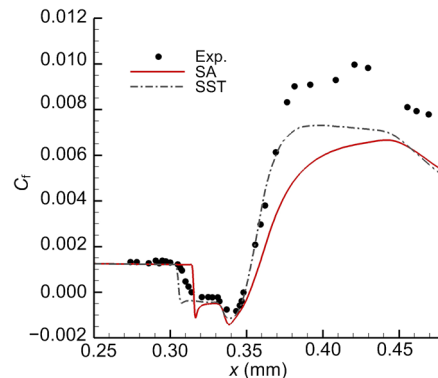


Fig. 6 Wall skin friction coefficient (C_f) distributions from SA and SST computational results compared with experimental data

$$u_{VD}^+ = \int_0^{u^+} \left(\frac{\rho}{\rho_w} \right)^{1/2} du^+, \quad (14)$$

where ρ_w is the wall density, μ_w is the wall viscosity, μ_τ is the friction velocity, and u_{VD}^+ is the van Driest transformed velocity.

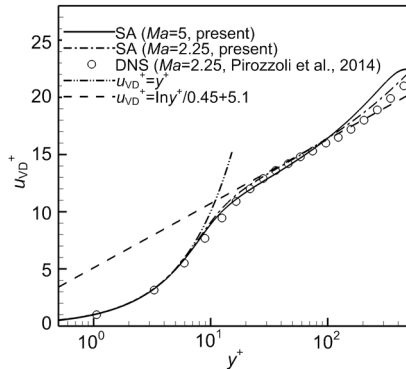


Fig. 7 Comparison of simulated velocity profiles with log law and DNS data

3 Overview of STBLI structure and MHD control

3.1 STBLI structure and MHD control

After the validation of STBLI computation results with experimental data, this section reviews the structure of the STBLI and MHD control types.

We began this work assuming that the flow is 2D and in a steady state. The schematic in Fig. 8 shows an incident shock-induced turbulent boundary layer separation. Incident shock penetrates into the separated viscous boundary layer and forms sharp adverse pressure gradients, resulting in a separation bubble. The start of STBLI is accompanied by the beginning of pressure fluctuation marked at point *I*. Separation starts at point *S* with the first steep pressure jump and ends at point *R* with a second slower pressure jump where the shear layer reattaches. The length from the separation point to reattachment is denoted as L_{Bubble} , while the free interaction length from the interaction starting point to the separation point is denoted as l_s .

Indeed, between leading and reattachment shock legs, there is a region of relatively uniform flow conditions inside the bubble, often characterized as a constant pressure plateau (John and Kulkarni, 2014) (Fig. 8).

To eliminate the adverse effects of STBLI, many methods of active control have been proposed (Narayanaswamy et al., 2012). Amongst the various factors that may determine the effectiveness of control in STBLI, several studies (Viswanath, 1988; Cuppoletti et al., 2016) on other active controls have revealed that control location is one of the critical factors. In the small diameter of the plasma arc (about 1 mm reported in the experiment), the MHD region is usually inside the boundary layer and does not extend into the core flow. In these circumstances, MHD control can be divided into four types:

U-type: MHD interaction is located upstream of where the separation point would have been without control;

S-type: MHD interaction is used across the separation point without control;

D-type: MHD interaction is inside the separation bubble and starts from the uncontrolled separation point;

R-type: MHD interaction is around the reattachment point.

We should examine the effects of MHD location in detail in the next section.

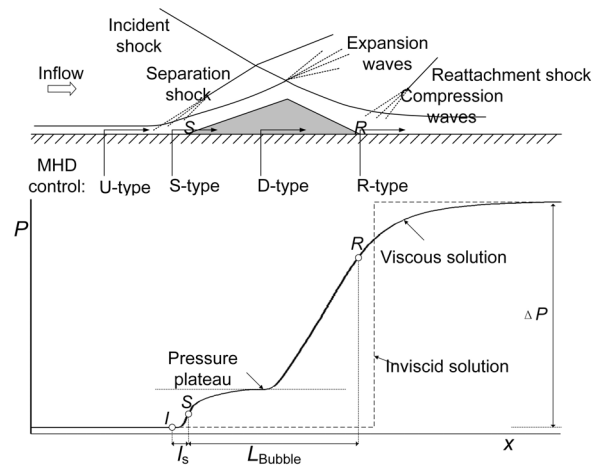


Fig. 8 Four types of MHD control positions of incident shock-induced turbulent boundary layer separation and wall static pressure

3.2 Interaction parameters governing MHD control performance

The effectiveness of MHD control is decided by the parameters, which are the key criteria for assessing the relative magnitude of the interactive forces. There are two classic magneto-aerodynamic similarity

parameters in all MHD research activities which depend on the interaction zone. The first parameter is the ratio of the ponderomotive (Lorentz force) and inertia forces of the core flow, also referred to as the Stuart number, S (Macheret et al., 2004), as follows:

$$S = \frac{\sigma B^2 L_{\text{MHD}}}{(1 + \Omega_e \Omega_i) \rho U_\infty}, \quad (15)$$

where Ω_e is the electron parameter and Ω_i is the ion Hall parameter. The effect of ion slip is so small ($\Omega_e \Omega_i \ll 1$) that it is neglected in this study; in the following description, U_∞ is the velocity of the main flow, and L_{MHD} is the length of the MHD region.

The second parameter is the ratio of ponderomotive (Lorentz force) and inertia forces of the boundary layer flow, written as follows:

$$S_\tau = \frac{\sigma B^2 L_{\text{MHD}}}{\rho U_\infty \sqrt{\frac{C_f}{2}}} = \sqrt{\frac{2}{C_f}} \times S. \quad (16)$$

The two parameters above are the defining indexes for conductive flow field with self-induced current. This means that there is no accessional current including the effect of direct current. In order to exert a robust and direction-specific accelerating influence on a designated location of a flow field with an electromagnetic force, an electric field is added to the arc discharge discussed in this paper. The parameter defining the additional electric field intensity is as follows:

$$k = -\frac{E_z}{U_\infty B}. \quad (17)$$

In this expression, the two parameters represented in Eqs. (15) and (16) can be converted into the following new forms:

$$S' = \frac{\sigma B^2 L_{\text{MHD}}}{\rho U_\infty} k, \quad (18)$$

$$S'_\tau = \frac{\sigma B^2 L_{\text{MHD}}}{\rho U_\infty \sqrt{\frac{C_f}{2}}} k = \sqrt{\frac{2}{C_f}} \times S \times k. \quad (19)$$

The classic MHD parameter in Eq. (18) shows the resistance of the dynamic pressure in the inviscid main flow with respect to the Lorentz force while the parameter in Eq. (19) describes the resistance of shear stress in the viscous boundary layer. The physical meanings of these two parameters seem inappropriate when it comes to controlling STBLI because they do not take the adverse pressure gradient into consideration.

It is important to define the correct scaling parameter regarding STBLI control. We present here a new approach for the analysis of a force balance inside the bubble, but neglect the effects of Joule heat in the same way as classic MHD parameters.

Fig. 9 shows the force balance in the x direction in the separation bubble of the STBLI structure under the control of Lorentz force. We present a simplistic analysis of parallel flow and just focus on the x -direction. Generally, the four main forces, including the dynamic pressure from momentum, adverse pressure gradient from the shock wave system, shear stress τ from the viscous effect of the shear layer, and the Lorentz force provided by the MHD plasma actuator, combine together to form a comparatively stable flow structure. The mathematical form for this can be expressed as

$$\frac{\partial}{\partial x}(\rho u^2) = -\frac{dp}{dx} + \frac{\partial \tau}{\partial y} + f_x. \quad (20)$$

Unsteadiness that exists in STBLI organization is associated with an acoustic feedback mechanism in the separation bubble (Threadgill and Bruce, 2016). The unsteadiness of the STBLI is not included in our time-averaged computations.

In the mathematical forms of classic MHD parameters, the ratio of Lorentz force and momentum or shear stress is taken into consideration. This is a reasonable assumption in cases where the MHD region remains in the main flow or is limited inside the boundary layer without separation.

However, because of the complexity in the STBLI structure, the classic parameters might not be effective in interpreting an inviscid-viscous interaction with a strong adverse pressure gradient manipulated by MHD force. In other words, the adverse pressure gradient is the main factor that outweighs momentum and shear stress, and thus it should be taken as reference when judging the effectiveness of

MHD control. Thus, the new MHD parameter is defined as follows:

$$S_{\Delta P} = -\frac{\sigma EBL_{\text{Bubble}}}{\Delta P}, \quad (21)$$

where ΔP denotes the pressure increase after an interaction which can be easily obtained from inviscid theory. In addition, uncontrolled separation bubble length L_{Bubble} can be predicted on the basis of the theory reported by Yao and Gao (2019) and Zhou et al. (2019) depending on the range of Reynolds number and Mach number or can be measured after the computational fluid dynamics calculation.

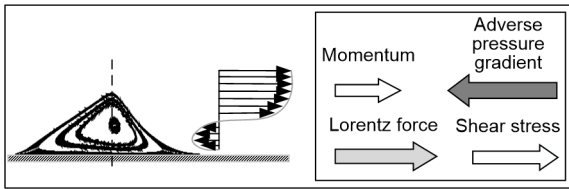


Fig. 9 Force balance of STBLI with MHD control in the x direction

4 Simulation results and discussion

4.1 Effect of MHD control types

Given a shock generator angle and hypersonic turbulent conditions upstream, MHD control performance would generally be subject to where the fluid is accelerated in relation to the separation point and how much total body force and heat deposit are applied. Four typical streamwise arrangements of MHD zones, corresponding to the four control types described in the previous section, and three typical arrangements of D-type with different distances perpendicular to the wall were investigated.

Fig. 10 shows the x -velocity contour of the baseline and four types of control flow field around the interaction. Similarly, Figs. 11 and 12 show the corresponding dimensionless wall pressure and friction coefficients, respectively, of the baseline and four types of MHD control with a magnetic strength of 4 T and a current intensity of 100 mA.

Fig. 10a shows the baseline flow field and the inviscid interaction point between incipient shock and wall is at $x=0$ mm. A bubble with a length of approximately 36.6 mm forms at about nine times the

length of the incoming turbulent boundary layer thickness δ_0 (about 4 mm), thus forming a typical STBLI.

The MHD zone in position 1 is illustrated in the solid frame of Fig. 10b. This U-type interaction manipulates the flow field by increasing momentum in the upstream boundary while decreasing the incoming turbulent boundary layer thickness δ_0 and the boundary layer displacement thickness δ_0^* . This effect can be interpreted by the theory of free interaction proposed by Chapman et al. (1958); in this formulation, the upstream separation length l_s from interaction start point x_0 to separation point x_s is proportional to the turbulent boundary layer displacement thickness δ_0^* , and is inversely proportional to the skin friction coefficient C_{f0} , and incoming Mach number Ma . This is defined as

$$l_s \sim \delta_0^* (C_{f0})^{-0.5} (Ma^2 - 1)^{-0.25}. \quad (22)$$

A decreasing δ_0^* enables the boundary layer with stronger resistance toward the adverse pressure gradient. In this type, because of thin plasma, MHD control does not make a difference unless the MHD region extends into the core flow where the upstream flow conditions mainly determine plateau pressure and STBLI separation bubble according to the inviscid analysis. As shown in Fig. 10b, the U-type MHD control at position 1 has little influence on the plateau pressure, and there is an increase in upstream skin friction coefficients, leading to a reduced separation length ratio that is the smallest among these four types.

The MHD zone in position 2, shown in the solid frame of Fig. 10c, stretches from upstream to the bubble across the separation point. The effects on STBLI of this S-type require fully coupled analysis of both the upstream and downstream effects around the separation point. There is a pressure leap at the end of the MHD zone inside the bubble (Fig. 11); this type decreases bubble length by a ratio of 0.265 according to results in Fig. 12.

The MHD zone in position 3, shown in the solid frame of Fig. 10d, is inside the separation bubble. This D-type MHD control shows the largest separation reduction, depicted in Fig. 10d, which reaches about 0.296. This is the best position for MHD control of STBLI.

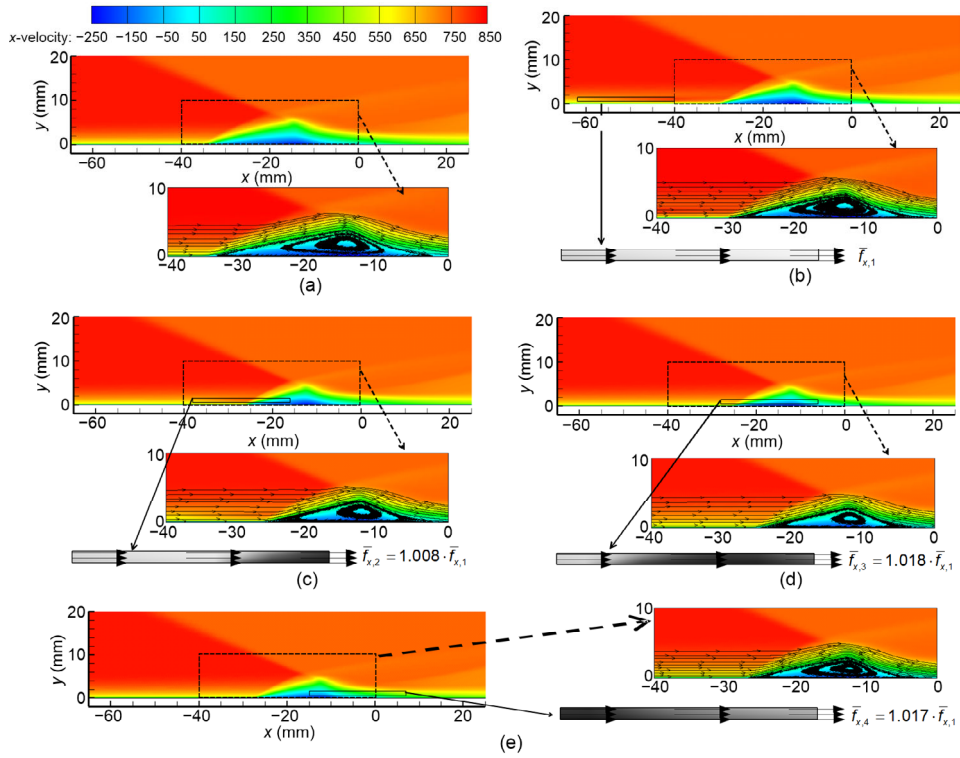


Fig. 10 X-velocity contour of baseline and four types of MHD control cases: (a) baseline; (b) position 1 (or U-type); (c) position 2 (or S-type); (d) position 3 (or D-type); (e) position 4 (or R-type)

$\bar{f}_{x,i}$ is the average value of Lorentz force in the x direction inside the MHD zone of each control position. Solid frames: magnified views of the Lorentz force vectors inside the MHD interaction zones; Dotted frames: magnified views of streamlines near the bubble

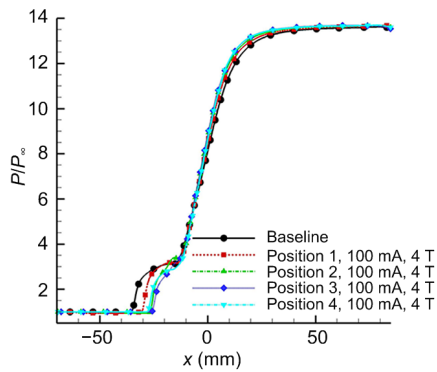


Fig. 11 Dimensionless wall static pressure distributions of baseline and four types of MHD control cases

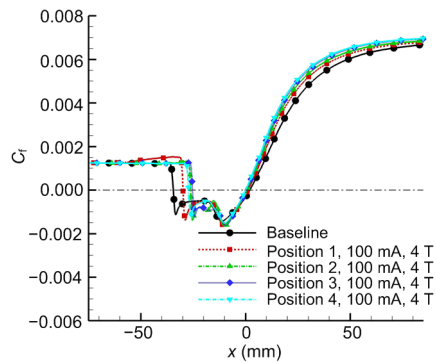


Fig. 12 Wall skin friction coefficient distributions of baseline and four types of MHD control cases

The MHD zone in position 4, shown in the solid frame of Fig. 10e, is across the reattachment point, and the upstream skin friction coefficient is unchanged because of the long distance from the separation point.

In terms of magnified views of streamlines near the bubble inside dotted frames and the Lorentz force

vectors inside the solid frames in Fig. 10, it is clear that position 3 (D-type) was the most appropriate. Inside the solid frames, arrows of Lorentz force vectors were applied; because the direction of the magnetic field is towards $y+$, these were only streamwise vectors. The darker the color inside the MHD zone is, the larger streamwise force is imposed. The average

value of Lorentz force inside the MHD zone is defined as follows:

$$\bar{f}_x = \frac{\iint f_x dx dy}{ab}. \quad (23)$$

The average value of Lorentz force in the x direction inside the MHD zone of each control position denotes as $\bar{f}_{x,i}$. It is clear that the average value of Lorentz force imposed in the D-type is slightly larger than the other, about 1.018 times of that in the U-type. This can also be confirmed by Eq. (4) because of the inverse flow. This direct enhancement of local flow inside the bubble helps to resist the adverse pressure gradient, postpone the separation point, and thus shrink the bubble, rather than accelerate the flow upstream and try to penetrate. In such a condition of comparatively high adverse pressure gradient in hypersonic STBLI flow and the limited size of the control zone, the vortex is not likely to be removed or shifted obviously according to the results from the four control types. Although the average values of Lorentz force imposed in D- and R-types are almost the same, the latter makes little difference to the movement of the reattachment point. Therefore, in order to obtain the minimum size of the bubble with a limited size of the MHD zone, it seems more effective to accelerate the boundary layer between the separation point and the vortex core.

We also compared our conclusions about the best MHD control streamwise position (best 'MHD control type' proposed in this paper) with the numerical results of Su et al. (2010). As flow conditions and size of the MHD zone are different in the two cases, short descriptions are listed in Table 2 to clarify the differences in supersonic/hypersonic and turbulent/laminar MHD control. It is noteworthy that Su et al. (2010) carried out a 2D supersonic simulation of MHD control on the oblique shock/laminar boundary layer interaction. Although the overall physics and topology of the two flows (oblique shock/laminar boundary layer interaction and oblique shock/turbulent boundary layer interaction) are the same, dramatic differences between laminar and turbulent flows render the nature of the incoming boundary layer an essential parameter. The length of the separation bubble in a laminar interaction is con-

siderably larger than that in a turbulent interaction (Babinsky and Harvey, 2011). Therefore, the ratio of MHD length to bubble length ($L_{\text{MHD}}/L_{\text{Bubble}}$) might differ by an order of magnitude although the length of the MHD zone we selected is almost the same as in (Su et al., 2010). The position of the MHD zone has to be selected precisely in the condition of a larger separation length. On the basis of Su et al. (2010), the best position to apply MHD is near the intersection point of the incident shock wave with the flat plate. As the shock angle in (Su et al., 2010) is 34.5° , this intersection point is located at the point where the pressure plateau is corresponding to our D-type. Therefore, it is better to decide the best control position according to the position of the bubble instead of the intersection point of the incident shock wave with the flat plate under different inflow conditions. As Mach number increases, it becomes harder to reduce the bubble size because of a larger pressure gradient.

In order to distinguish between thermal and body-force effects, plasma control with a 100 mA current was applied without the magnetic field. The summary in Fig. 13 shows the computed dimensionless wall static pressure distribution of the baseline and plasma control cases applied to the actuator in the absence of a magnetic field. These results agree with those from supersonic control simulations and experimental observations (Kalra et al., 2009); thermal energy in the MHD zone is not enough to significantly alter the static pressure profile.

The factor of wall distance to plasma actuation is also important; x -velocity profiles at four points, the dimensionless wall static pressure profile, and skin friction coefficient for the plasma actuator located 0.5 mm, 1.0 mm, and 2.0 mm from the wall are shown in Figs. 14, 15, and 16, respectively. Moving the plasma closer to the wall from freestream flow results in increased separation control. This shows that plasma actuation works best in the lowest-velocity region of the baseline; this leads to a smaller baseline shape factor as a result of the velocity profile at $x = -20$ mm (Fig. 14).

Results show that the most efficient MHD control is D-type, where the MHD interaction zone is inside the bubble and the plasma is set as close to the wall as possible. The next MHD parameter was analyzed using this D-type; wall distance in this case was set at 1 mm, corresponding to the experiment.

Table 2 Comparison of the best MHD positions

Study	Ma	Baseline	L_{MHD}/L_{Bubble}	Best position
Su et al. (2010)	2.0	Laminar	0.15	Near intersection point
Present	5.0	Turbulent	0.61	D-type

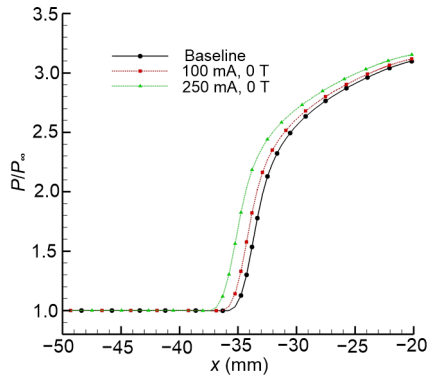


Fig. 13 Dimensionless wall static pressure distributions in baseline and plasma control cases

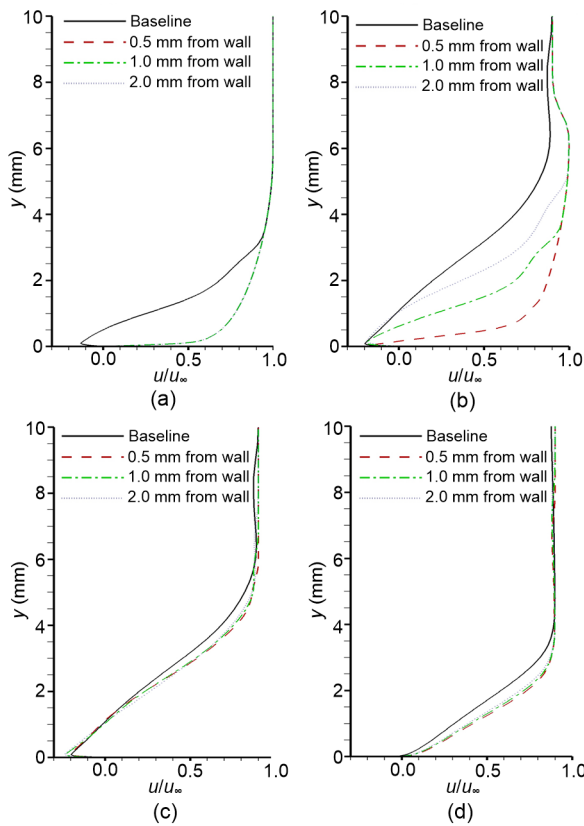


Fig. 14 X-velocity profiles at four points
(a) $x=-30$ mm; (b) $x=-20$ mm; (c) $x=-10$ mm; (d) $x=0$ mm

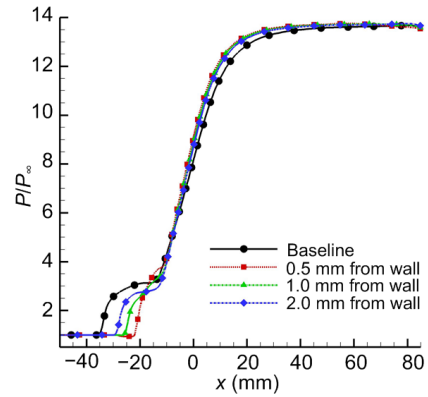


Fig. 15 Dimensionless wall static pressure distributions of baseline and MHD control at three different wall distances

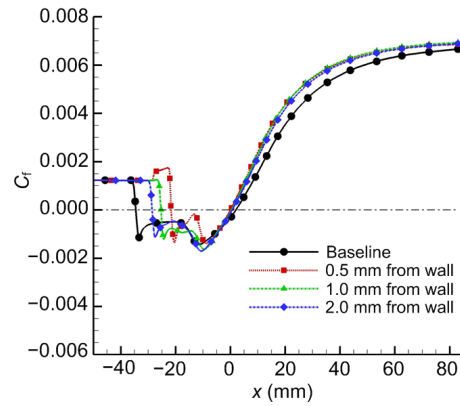


Fig. 16 Wall skin friction coefficient distributions of baseline and MHD control at three different wall distances

4.2 Effect of MHD parameter

In order to evaluate the parametric effect on bubble suppression of the MHD plasma actuators in high-speed STBLI flow fields, a new MHD interaction parameter was chosen to analyze the effectiveness of separation suppression.

As MHD control involves additional momentum and heat in the boundary layer, parameters affecting performance include the magnetic field intensity, plasma conductivity, and applied width b and height a in 2D flows. These parameters all influence body force (Lorentz force) and Joule heat effects. One certain $S_{\Delta P}$ value from a different combination of magnetic field intensity and plasma conductivity would result in a different amount of Joule heating.

Fig. 17 shows the dimensionless separation length L^* with MHD control under different electromagnetic inputs and L^* is defined as the ratio of MHD

controlled separation bubble length $L_{Control}$ to the uncontrolled separation bubble length L_{Bubble} . The strength of the MHD force and heat increase in consistent with parameter $S_{\Delta P}$ from 0.087 to 0.435, while a stronger reduction in the separated region can be inferred if $S_{\Delta P}$ continues to increase. In addition, we compared the difference of 100 mA and 200 mA with the same $S_{\Delta P}$ by adjusting the magnetic field intensity. Results show that a larger current can generate a greater Joule heat in the control zone, and thus it can be inferred that an unfavorable thermal effect would offset the momentum increase. Thus, the evaluation of MHD effects on the STBLI requires pre-judging the heating effects because the plasma arc alone is also used in the modification of flowfield structure, referred to as electrohydrodynamic (EHD) (Macheret et al., 2004). Indeed, as reported in some other studies on EHD control (Gan et al., 2018), the peak value of current can be as high as 100 A, enough to cause thermal accumulation or aerodynamic effects like plasma jets. In MHD control, however, these are unfavorable. In the process of MHD actuator design, the Lorentz force must be big enough to offset the thickening of the boundary layer caused by the thermal effect. Simulations can be done to help determine maximum thermal input.

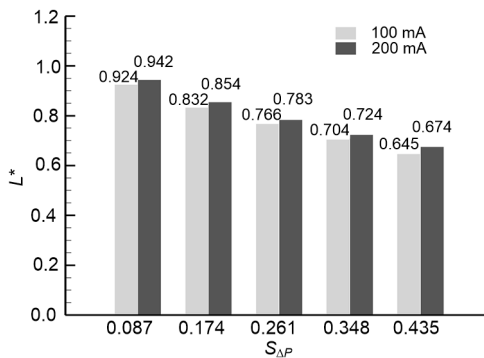


Fig. 17 Dimensionless separation lengths with MHD control at different electromagnetic inputs

Fig. 18 shows dimensionless pressure gradient distributions along the x -axis under different MHD parameters. The referred pressure gradient is $\Delta P/L_{Bubble}$. In an uncontrolled state, there are three zero points of the x -axis pressure gradient on the wall surface, marked A , B , and C . Point A is the boundary layer interaction starting point, where a reverse pressure gradient appears and the thickness of the

boundary layer increases to generate a series of compression wave systems. Once entering the reflow zone, in the inviscid fluid model (Souverein et al., 2013), the pressure gradient is regarded as zero. This pressure gradient cannot be immediately reduced to zero because of the effect of viscosity. This means that there is a much smaller isobaric area inside the bubble organization, limited between separation and reattachment points. We mark this zero point as B , where the pressure reaches a plateau. Thereafter, the separation streamline continuously decelerates until it stagnates at the R point as shown in Fig. 8. This process is accompanied by a compression wave system near the R point, so that the wall pressure gradient increases again and slowly decreases to zero; this third point is marked C .

D-type MHD control was applied including Lorentz force in the x -axis and Joule heat that changes the structure of the STBLI. This causes detention of separation at point A , and a notable rise of the dimensionless pressure gradient at point B . In order to probe the underlying physics of the relationships of the Lorentz force and the adverse pressure gradient, the dimensionless pressure gradient distributions at the isobaric zone under different magnitudes of MHD interaction parameters are compared and plotted in Fig. 18.

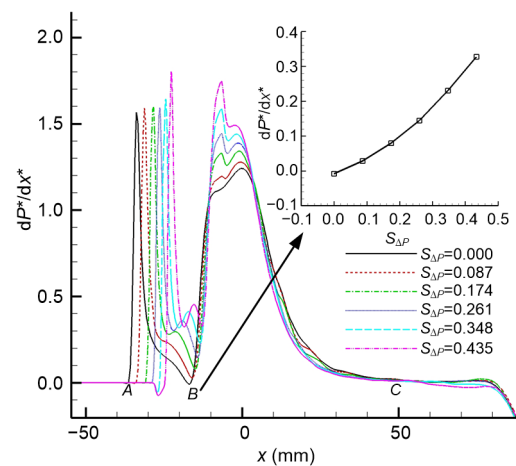


Fig. 18 Dimensionless pressure gradient distributions along the x -axis under different MHD parameters

It can be seen that the dimensionless pressure gradient at point B after control is of the same order as the MHD parameter, and that these maintain an approximately linear relationship with each other. The

new definition of MHD parameter adopted here equals the magnitude of the pressure uplift in the isobaric area to reach another force balance of STBLI organization and so the physical meaning is clearer. As the total increase of wall pressure caused by the STBLI remains constant and is not affected by the MHD control, the effectiveness of D-type control is closely related to the lift of the pressure gradient at the pressure plateau to exert a faster increase in pressure before the reattachment point.

5 Conclusions

We implemented a semi-empirical model based on experimental parameters of MHD plasma actuators into the RANS code at low magnetic Reynolds number approximation. Several cases, including MHD flow deceleration, STBLI of Mach 5 flow, and a compressible turbulent boundary layer, were first employed to validate our numerical method. We then summarized MHD interaction types based on the controlling position and proposed a new MHD interaction parameter. We then carried out a detailed study to examine the effectiveness and mechanism of MHD control. Conclusions can be drawn as follows.

1. Regarding MHD control techniques employing MHD plasma actuators, the effectiveness of this control depends on the location of control where the mechanisms can be different. The closer to the wall of the D-type MHD control, which is located at the isobaric zone in the separation bubble, the better the reduction of the STBLI separation length.

2. The pressure gradient of the isobaric zone in the separation bubble is approximately the same magnitude as the applied Lorentz force, and there is an approximately linear relationship between the pressure gradient and the Lorentz force after D-type MHD control.

3. The newly proposed MHD interaction parameter is clearer in its physical meaning and can be further applied to predicting the MHD controllability of STBLI.

Future work needs to address two issues encountered in this simulation. The first is further modification of the time-averaged model of plasma actuator based on data under different inflow conditions through experiments, and the other is the ap-

plication of MHD actuators to the more complex configurations like the inlets or wings of hypersonic vehicles. In this regard, according to the analysis of numerical results, what will be necessary next will be to increase the magnetic field intensity of the MHD zone and reduce weight at the same time. The solutions to the latter problem seem promising since the plasma used in the STBLI zone is so close to the surface where a larger magnitude of the magnetic field might be achieved by using electromagnets designed for the curved surface (Li et al., 2017b) or lighter magnets made of superconducting materials.

Contributors

Hao JIANG conducted the literature survey, wrote the first draft of the manuscript, and revised and edited the final version. Jun LIU put forward the original idea of the proposed classification framework and supervised the research activities. Shi-chao LUO and Jun-yuan WANG assisted with the literature survey, and document delivery and arrangement. Wei HUANG provided suggestions on the classification framework.

Conflict of interest

Hao JIANG, Jun LIU, Shi-chao LUO, Jun-yuan WANG, and Wei HUANG declare that they have no conflict of interest.

References

- Adamovich IV, 2010. Plasma dynamics and flow control applications. *In: Blockley R, Shyy W (Eds.), Encyclopedia of Aerospace Engineering*. John Wiley & Sons, Chichester, UK, p.1-9.
<https://doi.org/10.1002/9780470686652.eae042>
- Atkinson MD, Poggie J, Camberos JA, 2012. Control of separated flow in a reflected shock interaction using a magnetically-accelerated surface discharge. *Physics of Fluids*, 24(12):126102.
<https://doi.org/10.1063/1.4772197>
- Babinsky H, Harvey JK, 2011. *Shock Wave-boundary-layer Interactions*. Cambridge University Press, Cambridge, UK, p.28-36.
- Babinsky H, Li Y, Ford CWP, 2009. Microramp control of supersonic oblique shock-wave/boundary-layer interactions. *AIAA Journal*, 47(3):668-675.
<https://doi.org/10.2514/1.38022>
- Bisek N, Poggie J, 2013. Large-eddy simulations of separated supersonic flow with plasma control. Proceedings of the 51st AIAA Aerospace Sciences Meeting Including the New Horizons Forum and Aerospace Exposition.
<https://doi.org/10.2514/6.2013-528>
- Bisek NJ, Rizzetta DP, Poggie J, 2013. Plasma control of a turbulent shock boundary-layer interaction. *AIAA Journal*, 51(8):1789-1804.

- <https://doi.org/10.2514/1.j052248>
- Brown JL, 2011. Shock wave impingement on boundary layers at hypersonic speeds: computational analysis and uncertainty. Proceedings of the 42nd AIAA Thermophysics Conference.
<https://doi.org/10.2514/6.2011-3143>
- Chapman DR, Kuehn DM, Larson HK, 1958. Investigation of Separated Flows in Supersonic and Subsonic Streams with Emphasis on the Effect of Transition. Technical Report 1356, NACA, Moffett Field, USA.
- Cuppoletti DR, Saucier C, Harris C, 2016. Control of shock-induced boundary layer separation by high momentum blowing. Proceedings of the 52nd AIAA/SAE/ASEE Joint Propulsion Conference.
<https://doi.org/10.2514/6.2016-4763>
- Dietiker JF, Hoffmann K, 2002. Boundary layer control in magnetohydrodynamic flows. Proceedings of the 40th AIAA Aerospace Sciences Meeting & Exhibit.
<https://doi.org/10.2514/6.2002-130>
- Gaitonde DV, 2015. Progress in shock wave/boundary layer interactions. *Progress in Aerospace Sciences*, 72:80-99.
<https://doi.org/10.1016/j.paerosci.2014.09.002>
- Gan T, Wu Y, Sun ZZ, et al., 2018. Shock wave boundary layer interaction controlled by surface arc plasma actuators. *Physics of Fluids*, 30(5):055107.
<https://doi.org/10.1063/1.5013166>
- Huang W, Wu H, Yang YG, et al., 2020. Recent advances in the shock wave/boundary layer interaction and its control in internal and external flows. *Acta Astronautica*, 174: 103-122.
<https://doi.org/10.1016/j.actaastro.2020.05.001>
- John B, Kulkarni V, 2014. Numerical assessment of correlations for shock wave boundary layer interaction. *Computers & Fluids*, 90:42-50.
<https://doi.org/10.1016/j.compfluid.2013.11.011>
- Kalra CS, Shneider MN, Miles RB, 2009. Numerical study of boundary layer separation control using magnetogasdynamic plasma actuators. *Physics of Fluids*, 21(10): 106101.
<https://doi.org/10.1063/1.3233658>
- Kalra CS, Zaidi SH, Miles RB, et al., 2011. Shockwave-turbulent boundary layer interaction control using magnetically driven surface discharges. *Experiments in Fluids*, 50(3):547-559.
<https://doi.org/10.1007/s00348-010-0898-9>
- Kolev S, Bogaerts A, 2014. A 2D model for a gliding arc discharge. *Plasma Sources Science and Technology*, 24(1):015025.
<https://doi.org/10.1088/0963-0252/24/1/015025>
- Leonov S, Bituryn V, Savelkin K, et al., 2002. The features of electro-discharge plasma control of high-speed gas flows. Proceedings of the 33rd Plasmadynamics and Lasers Conference.
<https://doi.org/10.2514/6.2002-2180>
- Li K, Liu J, Liu WQ, 2017a. Mechanism analysis of magnetohydrodynamic heat shield system and optimization of externally applied magnetic field. *Acta Astronautica*, 133: 14-23.
<https://doi.org/10.1016/j.actaastro.2016.12.036>
- Li K, Liu J, Liu WQ, 2017b. Thermal protection performance of magnetohydrodynamic heat shield system based on multipolar magnetic field. *Acta Astronautica*, 136:248-258.
<https://doi.org/10.1016/j.actaastro.2017.02.011>
- Macheret S, 2006. Physics of magnetically accelerated nonequilibrium surface discharges in high-speed flow. Proceedings of the 44th AIAA Aerospace Sciences Meeting and Exhibit.
<https://doi.org/10.2514/6.2006-1005>
- Macheret SO, Shneider MN, Miles RB, 2004. Magnetohydrodynamic and electrohydrodynamic control of hypersonic flows of weakly ionized plasmas. *AIAA Journal*, 42(7):1378-1387.
<https://doi.org/10.2514/1.3971>
- Meyer R, Chintala N, Adamovich I, et al., 2004. Lorentz force effect on a supersonic ionized boundary layer. Proceedings of the 42nd AIAA Aerospace Sciences Meeting and Exhibit.
<https://doi.org/10.2514/6.2004-510>
- Narayanaswamy V, Raja LL, Clemens NT, 2012. Control of a shock/boundary-layer interaction by using a pulsed-plasma jet actuator. *AIAA Journal*, 50(1):246-249.
<https://doi.org/10.2514/1.j051246>
- Pirozzoli S, Grasso F, Gatski TB, 2004. Direct numerical simulation and analysis of a spatially evolving supersonic turbulent boundary layer at $M=2.25$. *Physics of Fluids*, 16(3):530-545.
<https://doi.org/10.1063/1.1637604>
- Poggie J, McLaughlin T, Leonov S, 2015. Plasma aerodynamics: current status and future directions. *Aerospace-Lab Journal*, (10):1-6.
<https://doi.org/10.12762/2015.AL10-01>
- Richard F, Cormier JM, Pellerin S, et al., 1996. Physical study of a gliding arc discharge. *Journal of Applied Physics*, 79(5):2245-2250.
<https://doi.org/10.1063/1.361188>
- Saito S, Udagawa K, Kawaguchi K, et al., 2008. Boundary layer separation control by MHD interaction. Proceedings of the 46th AIAA Aerospace Sciences Meeting and Exhibit.
<https://doi.org/10.2514/6.2008-1091>
- Schülein E, 2006. Skin friction and heat flux measurements in shock/boundary layer interaction flows. *AIAA Journal*, 44(8):1732-1741.
<https://doi.org/10.2514/1.15110>
- Shang JS, Surzhikov ST, 2005. Magnetoaerodynamic actuator for hypersonic flow control. *AIAA Journal*, 43(8):1633-1652.
<https://doi.org/10.2514/1.6625>
- Souverein LJ, Bakker PG, Dupont P, 2013. A scaling analysis for turbulent shock-wave/boundary-layer interactions. *Journal of Fluid Mechanics*, 714:505-535.

- <https://doi.org/10.1017/jfm.2012.495>
- Sriram R, Jagadeesh G, 2014. Shock tunnel experiments on control of shock induced large separation bubble using boundary layer bleed. *Aerospace Science and Technology*, 36:87-93.
<https://doi.org/10.1016/j.ast.2014.04.003>
- Su WY, Chang XY, Zhang KY, 2010. Effects of magnetohydrodynamic interaction-zone position on shock-wave/boundary-layer interaction. *Journal of Propulsion and Power*, 26(5):1053-1058.
<https://doi.org/10.2514/1.49838>
- Threadgill JA, Bruce PJ, 2016. Shock wave boundary layer interaction unsteadiness: the effects of configuration and strength. Proceedings of the 54th AIAA Aerospace Sciences Meeting.
<https://doi.org/10.2514/6.2016-0077>
- Viswanath PR, 1988. Shock-wave-turbulent-boundary-layer interaction and its control: a survey of recent developments. *Sadhana*, 12(1-2):45-104.
<https://doi.org/10.1007/bf02745660>
- White FM, 1991. *Viscous Fluid Flow*, 2nd Edition. McGraw-Hill, New York, USA, p.543-555.
- Yao Y, Gao B, 2019. Flow structure of incident shock wave boundary layer interaction with separation. *Acta Aerodynamica Sinica*, 37(5):740-747 (in Chinese).
- Zaidi S, Smith T, Macheret S, et al., 2006. Snowplow surface discharge in magnetic field for high speed boundary layer control. Proceedings of the 44th AIAA Aerospace Sciences Meeting and Exhibit.
<https://doi.org/10.2514/6.2006-1006>
- Zhang WH, Liu J, Ding F, et al., 2019. Novel integration methodology for an inward turning waverider forebody/inlet. *Journal of Zhejiang University-SCIENCE A (Applied Physics & Engineering)*, 20(12):918-926.
<https://doi.org/10.1631/jzus.A1900334>
- Zhou Y, Xia ZX, Luo ZB, et al., 2017. A novel ram-air plasma synthetic jet actuator for near space high-speed flow control. *Acta Astronautica*, 133:95-102.
<https://doi.org/10.1016/j.actaastro.2017.01.016>
- Zhou YY, Zhao YL, Zhao YX, 2019. A study on the separation length of shock wave/turbulent boundary layer interaction. *International Journal of Aerospace Engineering*, 2019: 8323787.
<https://doi.org/10.1155/2019/8323787>

中文概要

题目: 高超声速激波/湍流边界层干扰电磁控制研究

目的: 临近空间中下层巡航的新一代高超声速飞行器面临着高马赫数激波/湍流边界层干扰的问题。本文旨在探讨磁场/电弧放电耦合作用因素(焦耳热作用、放电参数、磁场强度、电弧作用流向位置和壁面距离等)对高马赫数工况下激波/湍流边界层干扰控制的影响,并提出激波/湍流边界层干扰洛伦兹力控制能力的参数表征,以揭示电磁控制的原理和能力。

创新点: 1. 建立低磁雷诺数假设下的激波/湍流边界层干扰数值模拟方法,对高超声速激波/湍流边界层干扰进行电磁控制,总结分析控制类型与控制机理,并根据仿真结果提出最佳控制参数建议。2. 建立针对激波/湍流边界层干扰的磁控能力预测参数,以指导高超声速飞行器典型激波/湍流边界层干扰的磁控设计。

方法: 1. 建立低磁雷诺数假设下的激波/湍流边界层干扰数值模拟方法,并分别对电磁力控制边界层、激波/湍流边界层干扰和湍流边界层速度剖面进行计算,验证使用方法的可靠性和有效性。2. 采用相关实验的电磁激励器的半经验模型,对二维稳态假设下的激波入射平板进行数值模拟,并研究电磁输入参数对分离区大小的影响。3. 通过理论分析,建立针对激波/湍流边界层干扰的磁控评价参数,并通过不同磁控强度下的数值仿真进行验证。

结论: 1. 四种电磁控制类型的控制机理和控制效果不同;电磁控制区位于分离泡内的等压区且距离壁面越近对减弱激波/湍流边界层干扰分离的效果越好。2. 电磁控制后等压区压力梯度与外加电磁力处于同一量级且呈近似线性关系。3. 本文所提出的磁控参数的物理意义更加明确,可进一步应用于对不同工况下激波/湍流边界层干扰分离控制的预测。

关键词: 高超声速; 激波/湍流边界层干扰; 磁流体; 流动控制